JOURNAL OF MATERIALS SCIENCE **38** (2003) 1185–1194

Damage zone interaction due to non-oriented Vickers indentations on brittle materials

W. ZHANG*, G. SUBHASH†
Department of Mechanical Engineering-Engineering Mechanics, Michigan Technological University, Houghton, MI 49931, USA
E-mail: subhash@mtu.edu

Induced damage in brittle materials due to two interacting Vickers indentations at various orientations was investigated using a three-dimensional finite element model. The model considers 'tensile cracking and compressive yielding' behavior of ceramics. Damage evolution due to both the simultaneous and sequential double indentations was studied. The simulation results indicated that the induced damage zone patterns are strongly a function of the relative orientation of the two indenters. The existence of another nearby indentation reduces the crack size on the side closer to the first indentation but increases the overall median damage zone size. These results were validated by sequential Vickers indentation experiments on borosilicate glass. The evolved damage patterns were further rationalized based on Bousinesq and blister field stress fields. Finally, the implication of these results on material removal mechanisms due to simultaneous interaction of several grits in a ceramic grinding process is discussed.

1. Introduction

Vickers indentation experiments have been widely used to model the material removal mechanism and to analyze the interaction between the diamond grits of a grinding wheel and a ceramic workpiece during a grinding process [1–3]. It has been well established that median cracks develop normal to the surface during the loading phase and lateral cracks develop parallel to the surface during the unloading phase of a Vickers indentation cycle [1]. The median cracks are viewed as the residual damage because they remain in the workpiece after grinding and the lateral cracks are considered to be responsible for the material removal. However, the damage evolution and the material removal process during grinding of brittle materials cannot be fully captured by a single indentation test because the induced damage is also strongly influenced by the interaction of the stress fields created simultaneously by several neighboring grits.

To more realistically depict the damage and material removal phenomena in a ceramic grinding process, scratching models [3–6], multi-indentation experiments [7, 8], and multi-scratch experiments [9] were employed in the literature. However, analytical models that take into account the material removal mechanisms and the interaction effects during ceramic grinding are difficult to develop due to the complicated stress fields created by the moving indenter or the interacting indentations and scratches. Thus, the experimental results usually have to be interpreted qualitatively or empirically. Finite element methods are being increasingly used to solve these complex problems and to gain a better insight into the stress distribution and the damage development during the indentation tests. Recently, Zhang and Subhash [10, 11] developed an 'elastic-plastic-cracking' (EPC) model that accounts for tensile cracking and compressive yielding of brittle materials and simulated single indentation and double indentation experiments. The model was found to capture the development of median cracks during the loading phase and the development of lateral cracks during the unloading phase of a Vickers indentation cycle [10]. The induced damage zone size was strongly influenced by the separation distance between the two diagonally-aligned indentations [11]. In the current work, the relative orientations of the two indenters were varied systematically to analyze their influence on the induced damage.

The motivation for the current work stems from the experimental observations of Choi and Salem [7] where, "repulsive" and "attractive" modes between the cracks created by two adjacent non-aligned Vickers indentations were noted. They found that irrespective of the orientations of the Vickers indenters, the cracks due to the second indentation were repulsed by the cracks due to the nearby first indentation for "as-indented" condition. The induced cracks due to the second indentation tend to be smaller on the side closer to the first indentation than those farther away. But the cracks created by the first and the second indentations were "attractive" when the specimen was annealed after the

* *Present address*: Graduate Aeronautical Laboratories, M/C 105/50, California Institute of Technology, Pasadena, CA 91125, USA.
† Author to whom all correspondence should be addressed.

first indentation. The resulting interaction modes were attributed to the residual stress field produced by the deformation mismatch between the elastic and plastic zones within the indentation imprint [7]. In a grinding process, the ground workpiece should be in the "as-indented" condition due to multi-loading of the diamond grits. Thus, the annealing effect was not considered in this investigation.

The paper is organized as follows. In Section 2 a brief description of the EPC constitutive model and the finite element descretization of the double indentation model are provided. The numerical results for the sequential and simultaneous indentations in various orientations are presented in Section 3. These results are validated by sequential indentation experiments on glass in Section 4. The resulting damage patterns are further analyzed in Section 5 by utilizing Bousinesq and Yoffe solutions for point loads. Finally, the implications of the results for ceramic grinding are discussed and conclusions are presented.

2. Model description

The elastic-plastic-cracking (EPC) model recently developed by Zhang and Subhash [10] has been successfully utilized to analyze indentation induced cracking in brittle materials. The model was also utilized to develop a 'brittleness measure' that characterizes the propensity for cracking in brittle materials. Since the complete details of the model are available elsewhere, only a brief description of the model is presented here for completeness.

Fig. 1 shows the EPC model, which includes a tensile linear elastic response OB followed by cracking and the associated stress release process BC. The point B represents the uniaxial tensile fracture strength of the material where cracking initiates. The line DE denotes the unloading followed by compressive loading from an arbitrary point D. Under compressive loading the material exhibits elastic-plastic response. The compressive yielding occurs when the stress exceeds the flow stress σ_e at point E. The 'tensile cracking and compressive yielding' behavior is typical of ceramic materials in indentation experiments. The plasticity associated with compressive stress during the loading phase of the indentation cycle is mainly responsible for subsequent lateral cracking during the unloading phase of the cycle [1]. The Mises flow stress σ_e during the plastic deformation is modeled as

$$\sigma_e = Y + E_p \varepsilon_e^p \tag{1}$$

Where Y is the uniaxial yield stress, E_p is the plastic hardening modulus and ε_e^p is the equivalent plastic strain.

Upon loading beyond the stress level σ_f, cracks will be initiated. The initiation of a crack at B is assumed to follow the maximum principal stress criterion. To account for the intensity of induced damage, a maximum of three orthogonal cracks are allowed to occur at any given material point. When the maximum principal stress at a given material point exceeds the predefined fracture stress σ_f, a mode I crack will appear normal to the maximum principal stress axis. After the initiation of the first crack, a second crack could occur only if the maximum tensile stress in the first crack's plane exceeds σ_f and a third crack could occur only if the tensile stress in a direction perpendicular to both of the above two crack normals exceeds σ_f. The normals to the three cracks form a local orthogonal coordinate system. Once a crack is initiated, its direction is not allowed to change and hence this is a 'fixed orthogonal crack model.' Upon cracking, stresses and strains are transformed into the local coordinate system. The normal stress t_i across a given crack i will be updated when it exceeds the current local fracture stress, which is assumed to be a power law function of the crack opening displacement u_i and is given by

$$t_i = \sigma_f f_i \ (i = 1, 2, 3), \quad \text{where} \ \ f_i = (1 - u_i/u_0)^n. \tag{2}$$

Here σ_f is the uniaxial macroscopic fracture stress, and u_0 and n are assumed to be material constants. In this paper, u_0 is assumed to be the maximum crack opening displacement (COD) (at C in Fig. 1) and is taken to be 5 μm based on the experimental work of Yu and Kobayashi [12] on ceramic matrix composites. The parameter n controls the shape of the post-cracking (stress release) curve BC and is assumed to be parabolic in nature with $n = 2$.

The COD u_i at a given stress state is estimated by multiplying the cumulative cracking strain e_i by a characteristic length h [13], i.e.,

$$u_i = h e_i = h \int \mathrm{d}e_i \tag{3}$$

where, h is the cube root of the corresponding element volume, and $\mathrm{d}e_i$ is the incremental strain between two adjacent time steps during the cracking process at any material point. Once COD is calculated for a given crack under a given state of stress, the total damage magnitude at any material point is calculated by defining the effective COD u_d along the three orthogonal directions as per

$$u_d = \sqrt{u_1^2 + u_2^2 + u_3^2}. \tag{4}$$

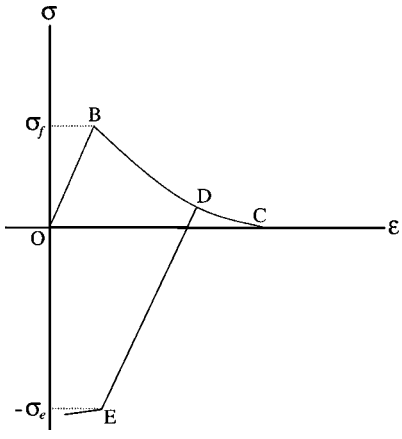

Figure 1 Elastic-plastic-cracking constitutive model for typical brittle materials.

Therefore, u_d represents the severity of damage at any material point for a given state of stress and is plotted in all the subsequent figures where damage characteristics are presented.

The shear stresses on a crack plane will also be released to zero upon cracking. To simplify the model, we assume the effective shear modulus G to be a function of the corresponding post-cracking functions f_i and f_j in two orthogonal directions as [10]

$$G = \frac{\mu f_i f_j}{f_i + f_j - f_i f_j} (i \neq j) \tag{5}$$

where, μ is the shear modulus of the uncracked material. Thus, in the local coordinate system, shear stress t_{ij} can be expressed as a function of the sum of the elastic and cracking strains

$$t_{ij} = 2G\left(e^e_{ij} + e^c_{ij}\right) = 2G\left(e_{ij} - e^p_{ij}\right) \tag{6}$$

where, e_{ij} is the total strain, e^e_{ij}, e^p_{ij} and e^c_{ij} are the strains due to elastic, plastic and cracking response of the material, respectively. The local stresses will be transformed back into the global system to calculate new displacements and strains for the next time step.

It should be pointed out that this model would reduce to the traditional Mises model if there were no cracking (for instance, when large fracture stress is used). Comparison between this model and the ABAQUS built-in Mises model has been conducted for single indentations. It was found that the simulation results in terms of total reaction force, stress distribution and strain distribution were identical in the absence of cracks.

The above model was successfully incorporated into the general-purpose finite element package ABAQUS/Explicit [13]. More details of the derivations of the above equations as well as the results of the simulations of the indentation cracking during a single Vickers indentation cycle can be obtained from the previous work of Zhang and Subhash [10].

As mentioned before, the focus of the current investigation is to analyze the effect of relative orientation of two indenters on the induced damage. The indenters are identified as $\mathcal{L}$ (for left indenter) and $\mathcal{R}$ (for right indenter) and the relative orientation of the two indenters was varied systematically in the simulations. Both the simultaneous and sequential indentations were considered to investigate the influence of loading sequence. In simultaneous indentations, the two indenters were loaded and unloaded at the same time, and in sequential indentations the second indenter was loaded only after the first indenter was completely unloaded.

The schematic of the double Vickers indentation model for one specific orientation is illustrated in Fig. 2, where the diagonals of the two indenters are aligned along the symmetric plane on a cylindrical specimen of 5 mm in diameter and 2.5 mm in length. All the nodes on the bottom surface of the specimen were constrained in the indentation direction as illustrated in the side view of Fig. 2. Due to the symmetry of the problem, only one half of the complete specimen was modeled with symmetric boundary conditions applied to the half plane. Typical ceramic material properties were used in the analysis, i.e., density $\rho = 3.2$ g/cm^3, Young's modulus $E = 320$ GPa, Poisson's ratio $\nu = 0.24$, tensile fracture stress $\sigma_f = 0.5$ GPa, compressive yield stress $Y = 5$ GPa, and plastic hardening modulus $E_p = 3.2$ GPa.

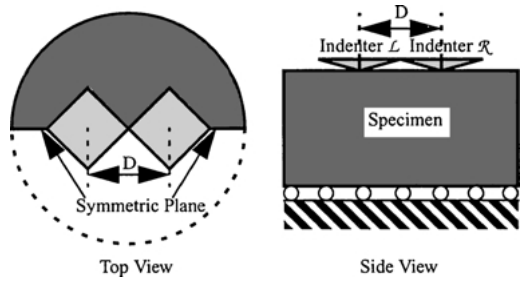

Figure 2 Schematic of double Vickers indentation model.

The Vickers indenter with an included angle of 136° was modeled as a rigid body consisting of five shell elements. An initial velocity of 33.3 m/s and a constant acceleration were applied to each indenter in the axial direction, which resulted in a maximum indentation depth (d) of 25 μm on the ceramic specimen in 1.5 μs (loading phase) and the indenter was pulled back to its original position in another 1.5 μs (unloading phase). So the total duration for an indentation cycle in simultaneous indentations is 3.0 μs and for sequential indentations it is 6.0 μs since the second indenter ($\mathcal{L}$) was loaded only after the first indenter ($\mathcal{R}$) was completely unloaded. The maximum indentation depth, d, for each indentation was kept constant at 25 μm and the distance between the two indenters (D) was kept at 300 μm. This separation distance was chosen based on the previous work of Zhang and Subhash [11] where the induced damage for two diagonally-aligned indenters was analyzed. It has been noticed that the interaction effect between the two indentations can be better visualized at a normalized distance of $D/d \approx 12$. In the current investigation the relative orientation of the two Vickers indenters was changed systematically as shown in Figs 3 and 4. The contact between the indenter and the specimen was assumed frictionless since friction was found to have no significant influence in indentation simulations [14].

In the region close to the indentation, a minimum element size of 12.5 μm was used in the specimen. Coarser mesh was used at distances farther away to reduce the computation time. This mesh size has been shown to result in a convergent solution for simulating the Vickers indentation test [11]. The simulations were performed on the SGI/CRAY Origin 2000 supercomputer at the University of Illinois at Urbana-Champaign. To avoid numerical instabilities due to cracking, the time step determined by ABAQUS was further reduced by 30%. The typical computation time was about 60 hours for each specific orientation presented in the following sections.

The need for the use of ABAQUS/Explicit code is clearly based on the fact that implicit static schemes cannot account for inertial effects and rate-sensitivity of materials (though rate-sensitive model has not been considered in the current work). The accuracy of

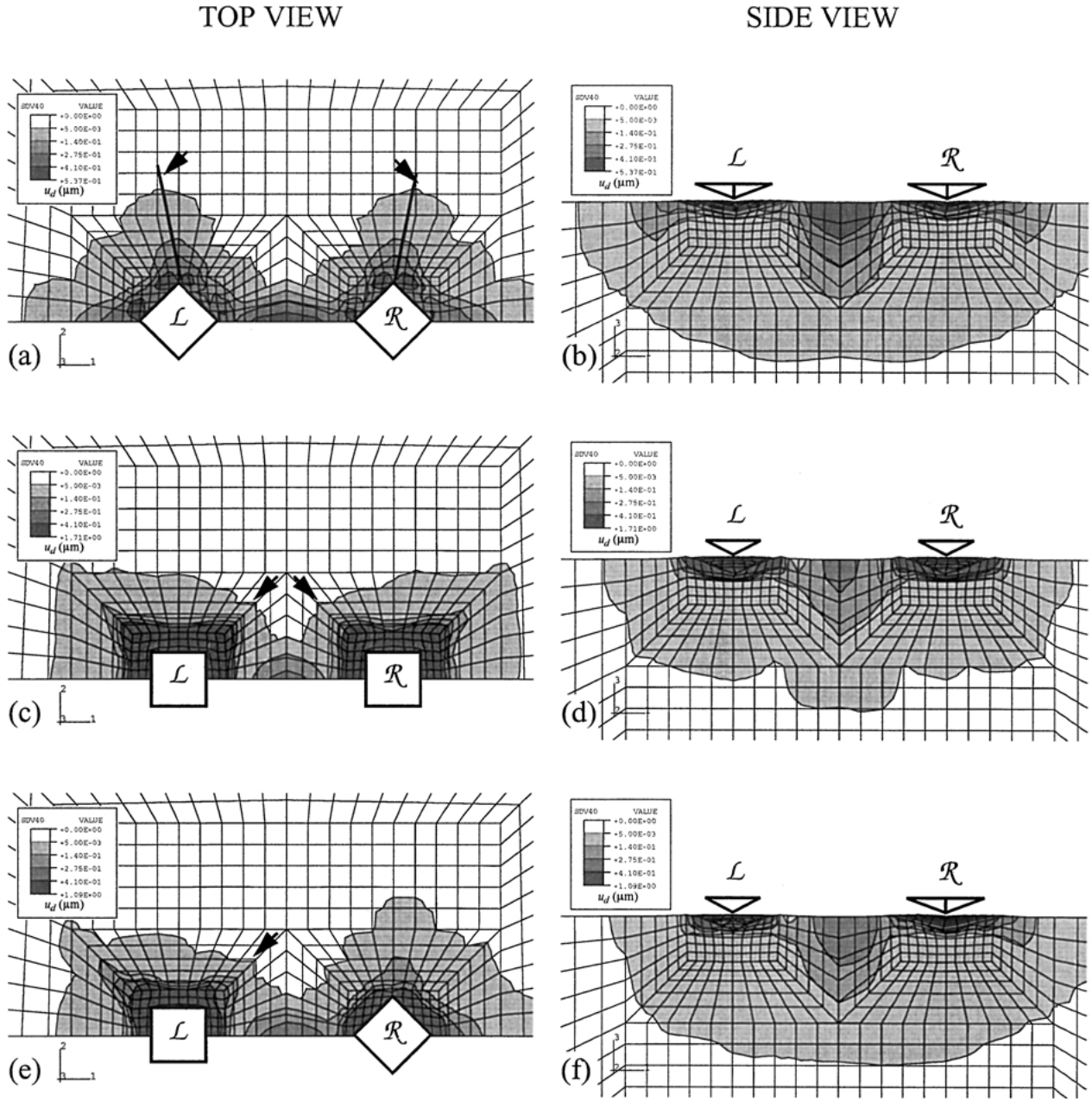

Figure 3 Induced damage zones due to simultaneous Vickers indentations revealing lateral damage (top view) and median damage (side view) in different indenter orientations. The arrows indicate "repulsive" mode of cracking due to the adjacent inentation.

explicit code has been carefully considered by using "double precision" instead of "single precision" and by decreasing the time step to make the solution converge. It has been shown that if the loading duration is long enough in explicit (when inertial force can be neglected), the indentation results from static code ABAQUS/Standard are identical to the results of ABAQUS/Explicit. Another reason for using explicit code is that we considered finite deformations to capture the strains associated with cracking [10]. In the interface of subroutine VUMAT, the incremental strains are provided in each step. The rigid body movement (or rotation part) has been removed from the total strains. Thus the strains used are purely due to deformation. In our model, the relationship between stress and strain is based on incremental strain but not the total strain. More details of these formulations are provided in Ref. [10]. It is emphasized that the intent of this approach is to capture the cracking phenomena due to double indentations but not to provide any quantitative information in terms of exact crack lengths or the magnitude of stresses.

3. Simulation results

3.1. Simultaneous indentations

Fig. 3 presents the induced damage zones upon complete unloading (3 μs) due to two simultaneous indentations for three different indenter configurations. Figs 3a and b show the top view (lateral damage) and the side view (median damage) of the damage contours (i.e., effective crack opening displacement u_d, see Equation 4), respectively, when the diagonals of the indenters $\mathcal{L}$ and $\mathcal{R}$ were aligned along the symmetric plane. It is seen that the induced damage zone is symmetric with respect to the central plane in between the two indentations. Two distinct damage zones corresponding to the two indenters can be identified from the top view

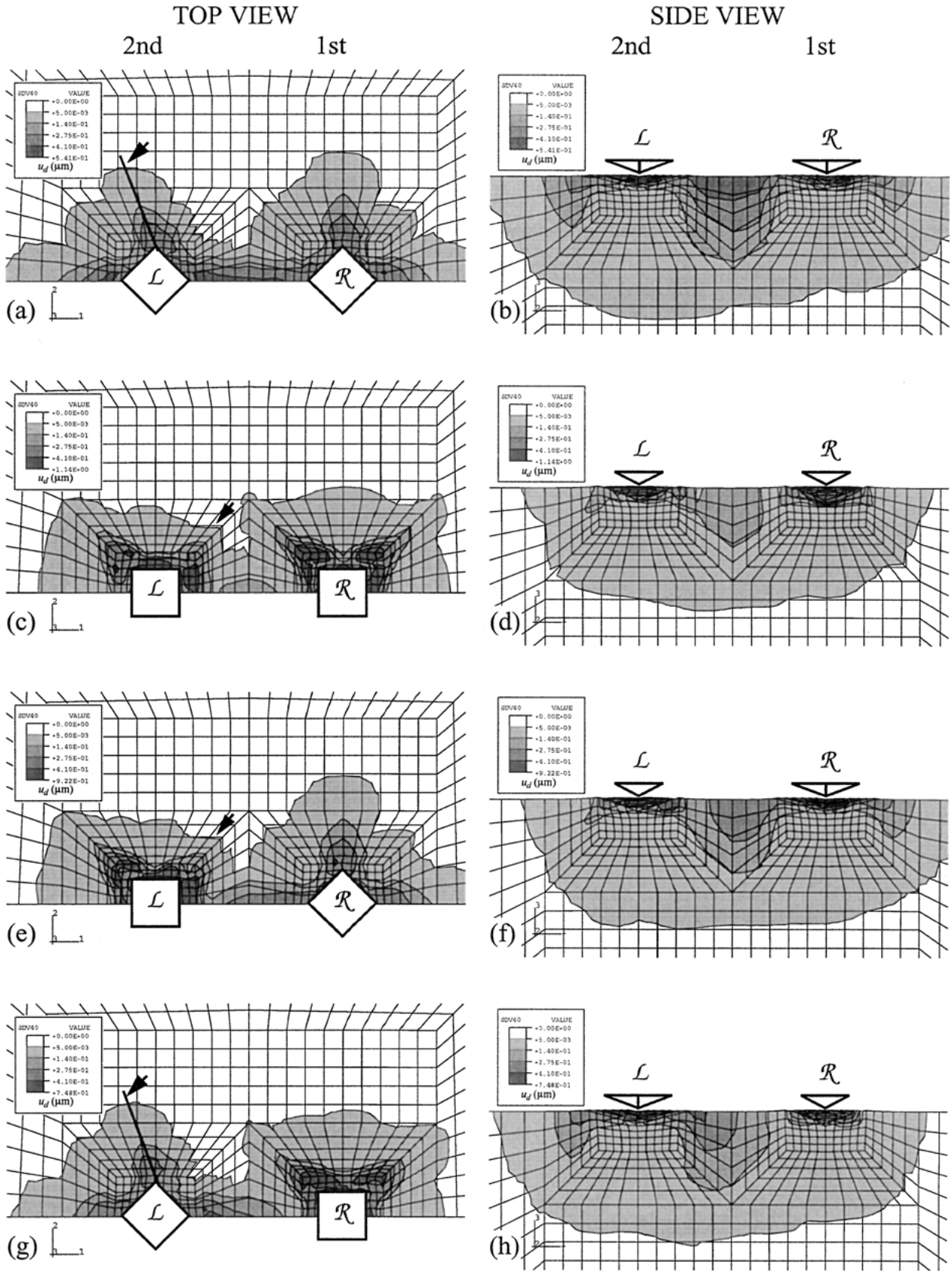

Figure 4 Induced damage zones due to sequential Vickers indentations revealing lateral damage (top view) and median damage (side view) in various indenter configurations. Indenter $\mathcal{L}$ was loaded only after indenter $\mathcal{R}$ was unloaded. The arrows indicate the "repulsive" mode of cracking.

(Fig. 3a), but the damage zones connect to form a single damage zone beneath the surface as seen in the side view (Fig. 3b). Note that a larger zone of intense damage is created in the central region in between the two indentations. It is interesting to note that the maximum damage zone size does not occur directly along the vertical diagonals of the indenters as indicted by arrows (in Fig. 3a) but shifts slightly outward. This mode of damage development differs from that due to a single indentation or due to two non-interacting indentations where, the maximum damage zone size always occurs along the diagonals [10, 11]. Therefore, the two damage

zones (along the diagonals in the top view) appear to be "repulsive" similar to the results of Choi and Salem [7]. In Figs 3c and d, both the indenters were rotated by 45 degrees relative to the previous orientation. The induced damage zone is once again symmetric with respect to the central plane in between the two indenters. The lateral damage zone size (Fig. 3c) along the corners facing the adjacent indentation (identified by the arrows) is significantly smaller than the damage zone size created along the corners facing away from the two indentations. Once again, this is clearly due to the "repulsive" mode of crack interactions [7]. On the other hand, the median damage zone on the plane in between the two indentations in Fig. 3d was larger than that created beneath each of the indenters. Finally, when the diagonal of indenter $\mathcal{R}$ was aligned along the symmetric plane and the orientation of the indenter $\mathcal{L}$ remained the same as in Fig. 3c, the induced damage shown in Figs 3e and f can be viewed as an intermediate situation between the previous two configurations. Once again, the damage due to the indenter $\mathcal{L}$ along the diagonal facing the indenter $\mathcal{R}$ is significantly smaller (as indicated by the arrows in Fig. 3e) than the diagonal facing away from the indenter $\mathcal{R}$, which further validates the "repulsive mode" of cracking [7].

It should be noticed that the maximum intensity of damage varies from 0.54 μm in Fig. 3a to 1.71 μm in Fig. 3c. The maximum damage intensity typically occurs directly beneath the indenters because the sharp edges of the pyramidal indenter would result in highly distorted mesh, especially when the indenters were oriented as shown in Fig. 3c. Therefore, additional constraints were imposed on those nodes directly beneath each indenter, i.e., the x displacement (along the symmetric plane, i.e., axis 1 in Fig. 3) of the mid node of three adjacent nodes was constrained to be the average of the x displacements of the two neighboring nodes. Due to the orientation of the indenters in Fig. 3c, similar constraint was applied to all those nodes on top surface that lie directly beneath the two indenters. Therefore, higher damage will develop due to these extra constraints in Fig. 3c than in Fig. 3a as more constraints were needed in Fig. 3c to maintain the quality of the final mesh. Hence, the maximum damage intensity is artificially altered in the local regions directly beneath the indenters. However, the effect of these extra constraints diminishes rapidly away from the regions close to the indenters and the damage developed farther away from the indenters as well as the damage intensity in the central region in between the two indentations is still valid and is solely due to the interaction of the induced stress fields.

3.2. Sequential indentations

The results of the simulations due to sequential indentations at various relative orientations are shown in Fig. 4. Here the right indenter $\mathcal{R}$ was loaded and unloaded first. The left indenter $\mathcal{L}$ was loaded only after the first indenter was completely unloaded. Because of this sequence, four indenter configurations arise as shown in Fig. 4. Once again, in all the configurations, the existence of the damage zone due to the first indentation strongly influences the damage pattern due to the second indentation. The induced damage due to the second indentation on the side closer to the first indentation is repulsed as indicated by arrows in all the four configurations. Hence the damage zone is either smaller (Fig. 4c and e) or is shifted away from the diagonals (as indicated by the lines that connect the contours of maximum damage intensities in Fig. 4a and g) during the second indentation. There are some additional differences compared to the damage zones presented in Fig. 3 for simultaneous indentations. Compared to Fig. 3a, c and e, the first indentations by the indenter $\mathcal{R}$ created larger lateral damage zone sizes as shown in Fig. 4a, c and e, respectively, than the second indentations by the indenter $\mathcal{L}$. The induced lateral damage zone sizes by the second indentations in Fig. 4a, c and e are similar to those created by the indenter $\mathcal{L}$ in simultaneous indentations in Fig. 3a, c and e, respectively, which imply that the preexisting residual stress field (by the indenter $\mathcal{R}$ in sequential indentations) and the coexisting stress field (by the indenter $\mathcal{R}$ in simultaneous indentations) have similar effect on the development of lateral damage. Contrary to the lateral damage zone sizes, the median damage zone size due to the second indentation (by the indenter $\mathcal{L}$) tends to be slightly larger than that created by the first indentation (by the indenter $\mathcal{R}$), especially when the indenters were oriented as in Fig. 4b. Finally, when the diagonal of the second indenter ($\mathcal{L}$) was aligned along the symmetric plane and the first indenter ($\mathcal{R}$) was rotated 45 degrees away from the indenter $\mathcal{L}$ (Fig. 4g), the resulting damage zone contour appears to be the combination of the damage zones due to the indenter $\mathcal{L}$ in Fig. 4a and due to the indenter $\mathcal{R}$ in Fig. 4c.

4. Experimental validation

To validate the trends in the induced damage observed in the above numerical simulations, i.e., repulsive modes of cracking, experiments were conducted on Borosilicate glass using a Vickers indenter. The validation was performed using sequential indentations, as they require only a single indenter on any commercially available hardness tester. Moreover, the alignment of the second indentation can be easily altered relative to the first by simply rotating the specimen after the first indentation. The indentations were performed at a load of 500 gms for 10 seconds (similar results were obtained at 300 gms). The distance between the indenters was maintained at around 50 microns.

Figs 5a–d present the results of the experiments for various orientations discussed before. In all these pictures the indentation on the right was performed first and the indentation on the left was performed second. In all the four cases, the first indentation developed median cracks of equal size along the four corners and the cracks are also aligned in line with the diagonals of the indentation. Upon second indentation, where the diagonals of the two indentations are aligned (Fig. 5a), the vertical cracks produced by the second indentation tend to repulse away from those produced by the first indentation thus clearly confirming the numerical predictions shown in Fig. 4a. Similarly, in the remaining three

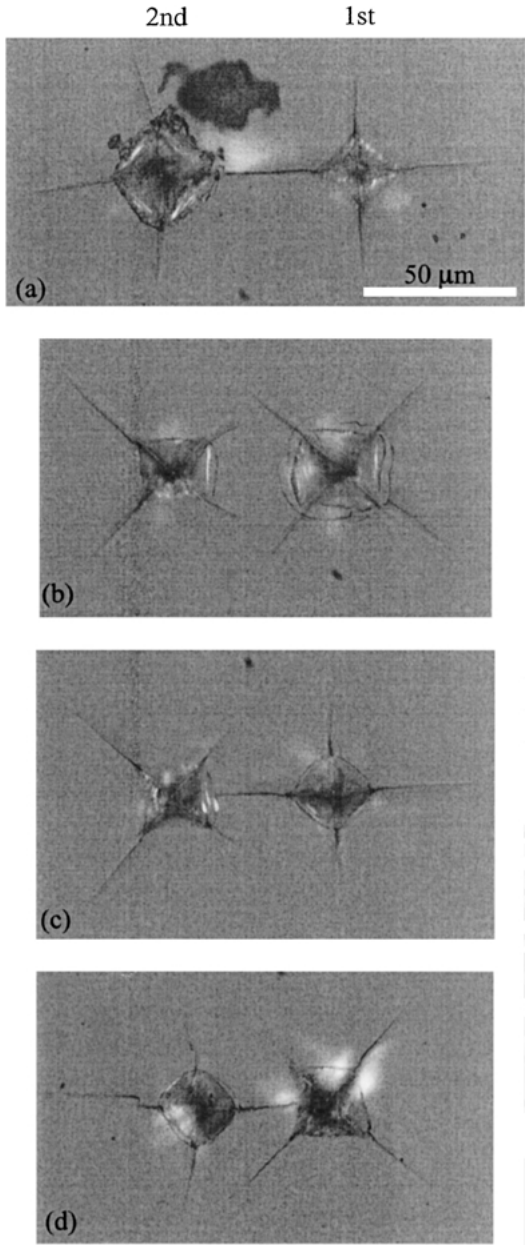

Figure 5 Experimental validation of "repulsive" mode of cracking between adjacent indentations in sequential double indentations. The indentation on the right was performed first and the one on the left was performed second. See Fig. 4 for corresponding numerical comparisions.

cases (Fig. 5b to d), the cracks induced by the second indentation tend to be either shorter on the side closer to the first indentation or deflect away from the first indentation, once again confirming the existence of repulsive mode of cracking and the numerical predictions. In addition, the cracks induced by the second indentation on the side away from the first indentation tend to be of the same size of those in the first indentation indicating that there is little effect of the residual stress filed induced by the first indentation. Clearly, all the above experiments validate the numerical simulations effectively for sequential indentations.

5. Discussions

In both simultaneous (Fig. 3a, c and e) and sequential indentations (Fig. 4a, c, e and g) the existence of a nearby damage zone (or the associated residual stress field) results in a smaller lateral damage zone size on the side closer to the adjacent indentation. This result is consistent with the experimental observations where "repulsive" interaction mode is operative between two adjacent indentations on glass. As seen in the results of sequential indentations above (Fig. 4), the first indentation created a larger lateral damage zone than the second indentation. This means that the unloading process in the first indentation is helpful for lateral crack development and thus facilitates the material removal process in grinding of ceramics. The simulation results further indicate that the damage zone size beneath the surface can be further increased by the interaction between two adjacent indentations. These damage zones tend to connect with each other and form a single large damage zone in both simultaneous (Fig. 3b, d and f) and sequential indentations (Fig. 4b, d, f and h). Also, higher damage intensity seems to develop in the central region in between the two indentations because of the interaction effects irrespective of the indenter orientations as well as whether the indenters were loaded simultaneously or sequentially. Moreover, the interaction effect was maximized when the indenters were both aligned diagonally along the symmetric plane. The effect of separation distance and the intensity of induced damages for diagonally aligned indenters were earlier analyzed by Zhang and Subhash [11]. In the following discussions we will try to explain the simulation results by further analyzing the analytical solutions due to point loads.

The damage zone evolution is a direct result of the stress field interactions of the two indenters [10, 11]. Boussinesq stress field and Yoffe's blister stress field [15] have been successfully used to predict the initiation and propagation of median cracks and lateral cracks during normal indentation experiments [16, 17]. During the loading phase of one indenter, the stress field generated can be expressed in the spherical polar coordinate system (see Fig. 6a) as [17]

$$\begin{cases} \sigma_{rr} = \dfrac{P}{2\pi r^2}\left[1 - 2\nu - 2(2-\nu)\cos\theta\right] \\ \sigma_{\theta\theta} = \dfrac{P}{2\pi r^2}\dfrac{(1-2\nu)\cos^2\theta}{1+\cos\theta} \\ \sigma_{\phi\phi} = \dfrac{P(1-2\nu)}{2\pi r^2}\left(\cos\theta - \dfrac{1}{1+\cos\theta}\right) \\ \tau_{r\theta} = \dfrac{P(1-2\nu)}{2\pi r^2}\dfrac{\sin\theta\cos\theta}{1+\cos\theta} \end{cases} \tag{7}$$

where, P is the instantaneous point load (or the total indentation load) applied to the flat surface, and ν is the Poisson's ratio of the specimen material.

When two indenters were loaded simultaneously, there will be two superposed Boussinesq stress fields (Equation 7) affecting the initiation of cracks. Fig. 6a illustrates the coordinate system used to explain the stress state due to two point loads. To simplify the analysis, let's consider a specific case, i.e., the stress state at a point M, which is located on plane xoz or x′o′z′ and the symmetric plane in between the two indentations. In this case, we have $r = \mathrm{r}'$ and $\theta = \theta'$, hence the

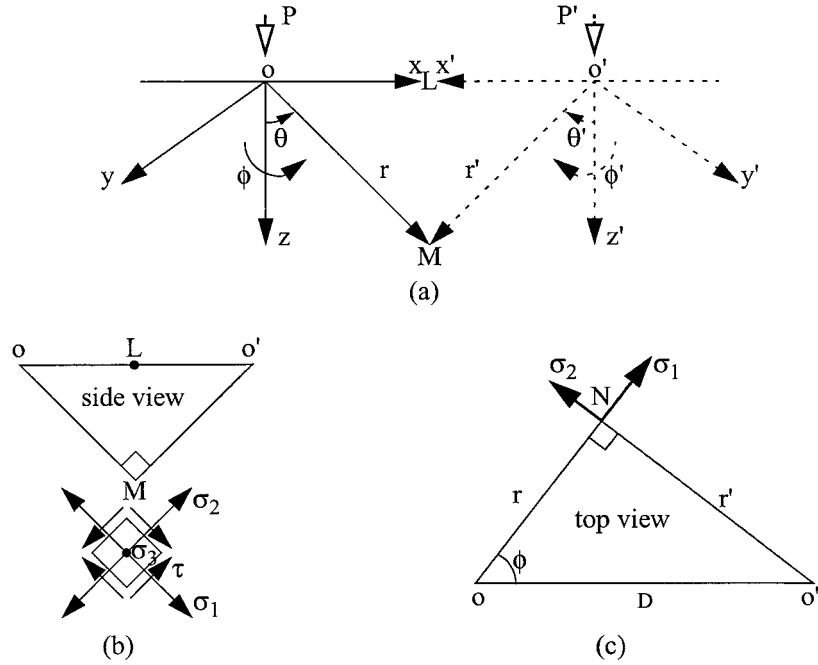

Figure 6 (a) Spherical polar coordinate systems for two indenters under normal indentation. Illustration of the stress status at a specific point (b) M below the top surface and (c) at N on the top surface of the specimen.

stress σ_3 (Fig. 6b) which is perpendicular to plane xoz is doubled ($\sigma_3 = 2\sigma_{\phi\phi}$). The σ_3 is the main contributor to initiate median cracks (normal to the top surface of the specimen), therefore, the doubled σ_3 will result in larger median cracks (or damage zone sizes). The finite element results (median damage zone sizes in Figs 3b, d and f) are consistent with the explanation based on the analytical model.

Since the initiation of micro cracks in the EPC model is due to the maximum tensile stress, which should be determined using all the stress components in Equation 7. To further validate the computational results, we can check two specific points, i.e., where the vector r is normal to the vector r′ ($r = $ r′ and $\theta = \theta' = 45^\circ$) and where the point M and the midpoint of oo′ (point L in Fig. 6b) coincide, i.e., $r = $ r′ and $\theta = \theta' = 90^\circ$.

At the first point ($r = $ r′ and $\theta = \theta' = 45^\circ$), the normal stresses σ_1 (along vector r) and σ_2 (along vector r′) are identical (see Fig. 6b). Using Equation 7 and bearing in mind that $\theta = \pi/4$ and assuming $\nu = 0.24$ the normal stresses σ_1 and σ_2 can be obtained using the following equations. Considering that the normal stress component σ_3 ($\sigma_3 = 2\sigma_{\phi\phi}$) and the shear stress component τ ($\tau = 2\tau_{r\theta}$) are both doubled at point M (note that r is normal to r′), the stress components under simultaneous indentations are

$$\begin{cases} \sigma_1 = \sigma_2 = \sigma_{rr} + \sigma_{\theta\theta} = \dfrac{P}{2\pi r^2}(-1.817) \\ \sigma_3 = 2\sigma_{\phi\phi} = \dfrac{P}{2\pi r^2}(0.126) \\ \tau = 2\tau_{r\theta} = \dfrac{P}{2\pi r^2}(0.305) \end{cases} \tag{8}$$

On the other hand, if there is only one indentation (e.g., the one on the left), the stress components at the same point M should be

$$\begin{cases} \sigma_1 = \sigma_{rr} = \dfrac{P}{2\pi r^2}(-1.969) \\ \sigma_2 = \sigma_{\theta\theta} = \dfrac{P}{2\pi r^2}(0.152) \\ \sigma_3 = \sigma_{\phi\phi} = \dfrac{P}{2\pi r^2}(0.063) \\ \tau = \tau_{r\theta} = \dfrac{P}{2\pi r^2}(0.152) \end{cases} \tag{9}$$

The principal stresses for double indentations calculated from Equation 8 are 0.126, −1.512, and −2.122 times $P/2\pi r^2$, respectively. For single indentation, the principal stresses (calculated from Equation 9) are 0.063, 0.163, and −1.980 times $P/2\pi r^2$, respectively. In the case of a single indentation, the maximum tensile stress $0.163P/2\pi r^2$ (in the plane of xoz) will cause cracking similar to the cone cracks [1]. However, double indentations seem to create merely median cracks at the same point M and its vicinity because only the stress normal to plane xoz is tensile (i.e., $0.126P/2\pi r^2$) and hence the median damage zone size was increased in the finite element analysis. According to the calculations from Equations 8 and 9, single indentation should introduce more damage than double indentations at point M (where $r = $ r′ and $\theta = \theta' = 45^\circ$) because the maximum tensile stress is higher in single indentation than in double indentations. But this may not be true when the point M is lowered further (i.e., $\theta = \theta' < 45^\circ$). Therefore, the resulting larger median damage zone in numerical simulations due to double indentations should not be a surprise. In fact, the stress state in finite element simulations is too complicated to explain quantitatively by the simple form of Boussinesq stress field.

At the second point L in Fig. 6b, where $r = \mathrm{r}'$ and $\theta = \theta' = 90^\circ$, the normal stresses σ_1 ($\sigma_1 = 2\sigma_{rr}$) and σ_3 ($\sigma_3 = 2\sigma_{\phi\phi}$) are doubled, the normal stress σ_2 and the shear stress τ are zero according to Equation 7. Thus, higher damage accumulates in between the central region of the two indentations.

During unloading the stress field for one indentation is the combination of Boussinesq solution and Blister solution [17]

$$\begin{cases} \sigma_{rr} = \dfrac{P}{2\pi r^2}[1 - 2\nu - 2(2-\nu)\cos\theta] \\ \qquad + \dfrac{4B}{r^3}[(5-\nu)\cos^2\theta - (2-\nu)] \\ \sigma_{\theta\theta} = \dfrac{P}{2\pi r^2}\dfrac{(1-2\nu)\cos^2\theta}{1+\cos\theta} - \dfrac{2B}{r^3}(1-2\nu)\cos^2\theta \\ \sigma_{\phi\phi} = \dfrac{P(1-2\nu)}{2\pi r^2}\left(\cos\theta - \dfrac{1}{1+\cos\theta}\right) \\ \qquad + \dfrac{2B}{r^3}(1-2\nu)(2-3\cos^2\theta) \\ \tau_{r\theta} = \dfrac{P(1-2\nu)}{2\pi r^2}\dfrac{\sin\theta\cos\theta}{1+\cos\theta} + \dfrac{4B}{r^3}(1+\nu)\sin\theta\cos\theta \end{cases} \tag{10}$$

where, $B = \frac{0.102Gf(P_{\mathrm{peak}}/H)^{3/2}}{\pi(1-2\nu)}$ is a constant, P_{peak} is the peak load from which the unloading starts, H is the Vickers hardness, G is the shear modulus, and f (ranging from 0 to 1) is a factor that accounts for non-volume-conserving processes in the deformation zone. Again, for the second point ($r = \mathrm{r}'$ and $\theta = \theta' = 90^\circ$) in simultaneous double indentations, σ_1 ($\sigma_1 = 2\sigma_{rr}$) and σ_3 ($\sigma_3 = 2\sigma_{\phi\phi}$) are doubled, σ_2 and τ become zero. Thus, more damage develops in the central region of the two indentations during the unloading phase. Both the loading and the unloading of the indenters promote damage development in the central region, which results in the damage zones similar to Fig. 3b, d and f.

If a point N (Fig. 6c, where $\theta = \theta' = 90^\circ$) on the top surface of the specimen (plane xoy) is considered, we have $\sigma_{\theta\theta} = 0$ and $\tau_{r\theta} = 0$ for both loading (Equation 7) and unloading (Equation 10) in a single indentation. It has been shown that upon unloading $\sigma_{\phi\phi}$ becomes tensile and it is possible to cause marginal radial or median damage propagation, and σ_{zz} (normal to the top surface) is tensile beneath the surface and is responsible for lateral cracking [10, 17]. During the loading phase in simultaneous double indentations, $\sigma_{\theta\theta} = 0$ and $\tau_{r\theta} = 0$ at point N (Fig. 6c). However, in the individual spherical coordinate system for an individual indentation (e.g., the left one), the other two stress components can be obtained from Equation 7 as

$$\sigma_{rr} = -\sigma_{\phi\phi} = \frac{P}{2\pi r^2}(1-2\nu) \tag{11}$$

More specifically, let's consider when $r = D\cos\phi$ is perpendicular to $\mathrm{r}' = D\sin\phi$ as shown in Fig. 6c. The superposed stress components at point N due to simultaneous indentations can be easily obtained as

$$\sigma_1 = -\sigma_2 = \frac{P(1-2\nu)}{2\pi D^2}\left(\frac{1}{\cos^2\phi} - \frac{1}{\sin^2\phi}\right) \tag{12}$$

According to Equation 11, if there is only one indentation (the left one), the stress components at point N will be

$$\sigma_1 = -\sigma_2 = \frac{P(1-2\nu)}{2\pi D^2}\frac{1}{\cos^2\phi} \tag{13}$$

Thus the tensile stress is decreased in double indentations (Equation 12) compared to that in single indentation (Equation 13), which leads to a smaller radial/median damage zone size on the top surface during the loading phase.

Upon complete unloading, the instantaneous load $P = 0$ in Equation 10, $\sigma_{\theta\theta} = 0$, and $\tau_{r\theta} = 0$ at point N, and the stress components for each indentation (e.g., the left one) in its local coordinate system are

$$\begin{cases} \sigma_{rr} = \dfrac{4B}{r^3}(\nu - 2) \\ \sigma_{\phi\phi} = \dfrac{4B}{r^3}(1-2\nu) \end{cases} \tag{14}$$

For double indentations, the stress components at point N ($r = D\cos\phi$ and $\mathrm{r}' = D\sin\phi$) are

$$\begin{cases} \sigma_1 = \dfrac{4B}{D^3}\left(\dfrac{\nu-2}{\cos^3\phi} + \dfrac{1-2\nu}{\sin^3\phi}\right) \\ \sigma_2 = \dfrac{4B}{D^3}\left(\dfrac{1-2\nu}{\cos^3\phi} + \dfrac{\nu-2}{\sin^3\phi}\right) \end{cases} \tag{15}$$

For single indentation (the left one), the stress components at the same point N are

$$\begin{cases} \sigma_1 = \dfrac{4B}{D^3}\left(\dfrac{\nu-2}{\cos^3\phi}\right) \\ \sigma_2 = \dfrac{4B}{D^3}\left(\dfrac{1-2\nu}{\cos^3\phi}\right) \end{cases} \tag{16}$$

One can easily see that the tensile stress is decreased in double indentations (Equation 15) as opposed to that in a single indentation (Equation 16). Therefore, it can be concluded that the damage zone size on the top surface will be smaller in double indentations than in single indentation, just as shown in Fig. 3. This also implies that the damage zone size on the top surface in the finite element analysis (Figs 3a, c and e) may be better interpreted as the extension of radial or median cracks.

To analyze the sequential indentations, the Boussinesq stress field due to the loading of the second indenter can be superposed on to the Blister field due to the complete unloading of the first indenter, or the unloading stress field (Equation 10) and a Blister solution can be superposed to represent the stress field upon the unloading of the second indenter. This will make the computation more difficult but the procedure

of the analysis is similar to that for simultaneous indentations presented above. To more realistically represent the stresses under Vickers indentations, a model that takes into account both the plastic zone and the cracking response [18, 19] should be employed.

Both the finite element analysis and the stress field prediction indicate the interactions between two indentations will change the resulting stress distribution and hence the damage zone size. The orientations and loading sequences of the indenters (or grits on the grinding wheel) and the distance between indenters [11] can be optimized to increase the lateral cracking and minimize the median cracking. Thus, with appropriate design of grits on a grinding wheel higher material removal rate can be obtained with acceptable induced damage in a ceramic grinding process.

It should be emphasized that the above analytical solutions for Boussinesq and Blister fields are based on severe approximations such as point force loading, elastic material behavior and small deformation theory. However, the equations are used solely to analyze the elastic stress fields faraway from the indenter tip. This elastic stress field cannot be significantly affected by the local stress/strain/damage distribution near the indenter tip. The comparison between the finite element results and the analytical model is made mainly to explain how the cracks initiate due to the interacting tensile stresses during double indentations and no quantitative information has been drawn based on this discussion.

6. Conclusions

A three-dimensional finite element model that captures the tensile cracking and compressive yielding behavior of ceramics was used successfully to simulate the interactions of two Vickers indentations with various indenter orientations. Both simultaneous loading and sequential loading were considered. It was found that the existence of a nearby indentation-induced damage zone (or stress field) strongly influences the development of damage zones due to another Vickers indentation. In particular, repulsive mode of cracking persists between the two indentations. For both simultaneous indentation and sequential indentations, the lateral damage zone size will decrease but the median damage zone size will increase due to the interaction effect. The diagonal-aligned indenters tend to create a larger damage zone and higher damage intensity in the central region in between the two indenters. It is to be emphasized that the relative orientations of the indenters can only affect the local damage development but not the whole picture of the induced damage zone size and shape. The Boussinesq solution and the Blister solution were used to analyze the stress field due to simultaneous indentations, which confirm the results of the simulations.

Acknowledgements

The authors gratefully acknowledge the financial support provided by the U.S. National Science Foundation under Grant No. DMI-9610454. This work was partially supported by National Computational Science Alliance and utilized the NCSA SGI/CRAY Origin 2000 supercomputer at the University of Illinois at Urbana-Champaign (UIUC).

References

1. R. F. COOK and G. M. PHARR, *J. Amer. Ceram. Soc.* **73**(4) (1990) 787.
2. A. W. RUFF, H. SHIN and C. J. EVANS, *Wear* **181–183** (1995) 551.
3. S. MALKIN and T. W. HWANG, *CIRP Annals* **45**(2) (1996) 569.
4. O. DESA and S. BAHADUR, *Wear* **225** (1999) 1264.
5. G. SUBHASH, J. E. LOUKUS and S. M. PANDIT, *Mech. Mater.* (2001) in press.
6. I. ZARUDI, L. ZHANG and Y.-W. MAI, *J. Mater. Sci.* **31**(4) (1996) 905.
7. S. R. CHOI and J. A. SALEM, *ibid.* **28**(2) (1993) 501.
8. P. C. TWIGG, R. W. DAVIDGE, F. L. RILEY and A. FRANCO, *Philos. Mag. A* **74**(5) (1996) 1245.
9. H. H. K. XU, S. JAHANMIR and Y. WANG, *J. Amer. Ceram. Soc.* **78**(4) (1995) 881.
10. W. ZHANG and G. SUBHASH, *Int. J. Solids Struct.* **38**(34–35) (2001) 5893.
11. *Idem.*, *Acta Mater.* **49**(15) (2001) 2961.
12. C. T. YU and A. S. KOBAYASHI, *Ceram. Eng. Sci. Proc.* **14**(7) (1993) 273.
13. ABAQUS/Explicit User Manual, Version 5.8 (Hibbitt, Karlsson & Sorensen, 1998).
14. A. E. GIANNAKOPOULOS, P.-L. LARSSON and R. VESTERGAARD, *Int. J. Solids Struct.* **31**(19) (1994) 2679.
15. E. H. YOFFE, *Philos. Mag. A* **46** (1982) 617.
16. A. CHANDRA, K. WANG, Y. HUANG, G. SUBHASH, M. H. MILLER and W. QU, *J. Manu. Sci. Eng.* **122** (2000) 452.
17. K. WANG, PhD thesis Michigan Technological University, Houghton, MI, USA, 1998.
18. B. R. LAWN, A. G. EVANS and D. B. MARSHALL, *J. Amer. Ceram. Soc.* **63** (1980) 574.
19. S. S. CHIANG, D. B. MARSHALL and A. G. EVANS, *J. Appl. Phys.* **53**(1) (1982) 298.

Received 18 April
and accepted 25 November 2002